Check for updates

Atomic-Scale Defected HfS$_2$ Nanosheets: A Novel Platform Enhancing Photocatalysis

Amin Talebian-Kiakalaieh, Elhussein M. Hashem, Meijun Guo, Bingquan Xia, Jingrun Ran,* and Shi-Zhang Qiao*

Recently, novel 2D materials with fascinating characteristics are extensively applied to design/fabricate high-activity and cost-effective photocatalysts for solar-driven fuels/chemicals generation. Among these 2D materials, HfS$_2$ nanosheets (NSs) exhibit excellent features of large surface area, short bulk-to-surface distance, alterable band structures, and vast catalytic sites. Despite these features, no realistic experimental works on HfS$_2$-based materials are reported in photocatalysis field. Moreover, it is interesting but challenging to realize atomic-scale engineering of compositions/structures for novel 2D materials and to relate these atomic-scale characteristics with the element/space/time-resolved charge kinetics of 2D materials-based photocatalysts. Herein, for the first time, atomic-scale defected HfS$_2$ NSs are designed/synthesized. The as-synthesized HfS$_2$ NSs are combined with various photocatalysts to acquire novel HfS$_2$-TiO$_2$, HfS$_2$-CdS, HfS$_2$-ZnIn$_2$S$_4$, and HfS$_2$-C$_3$N$_4$ composites, respectively. Among them, HfS$_2$-CdS exhibits the highest rate (5971 µmol g^{-1} h^{-1}) on hydrogen (H$_2$) evolution in triethanolamine aqueous solution, together with obviously-enhanced rates on H$_2$ (2419 µmol g^{-1} h^{-1}) and benzaldehyde (5.11 mmol g^{-1} h^{-1}) evolution in benzyl alcohol aqueous solution. Various state-of-art characterizations reveal the element/space/time-resolved electron/hole kinetics in HfS$_2$-CdS composites, disclosing that these atomic-scale S vacancies temporarily trapping electrons to facilitate spatiotemporal electron–hole separation/transfer. This work paves avenues to atomic-scale design/synthesis of new 2D-materials-based photocatalysts for sunlight utilization.

1. Introduction

Adopting photocatalysis technique to convert renewable solar energy into fuels/chemicals is of great significance to resolve the global energy/environmental issues.[1–12] Realistic application of this technique rests with the development of high-activity, stable and cheap photocatalysts. In the past decades, tremendous novel 2D materials have been developed and applied in photocatalysis field due to their distinctive features.[13–27] Among these new 2D materials, HfS$_2$ nanosheets (NSs) stands out owing to the appealing characteristics: 1) controllable thickness and lateral sizes to regulate the electronic band structures for optimizing the light absorption abilities and electron–hole redox capacities; 2) 2D structure benefiting the charge transfer from bulk to surface; 3) abundant undercoordinated catalytic sites on the large surface boosting the redox reactions; 4) high surface area facilitating the combination with all sorts of nanoscale building blocks. Despite these fascinating attributes, up till now, only some theoretical computations of HfS$_2$-based photocatalysts were reported on this field.[28–31] To the best of our knowledge, no realistic experimental works on HfS$_2$-based materials are reported in photocatalysis field to date.

Regulating the atomic-scale structures/compositions of novel 2D materials to optimize the physicochemical features is of central importance to realize the outstanding photocatalytic performances in key reactions. Especially, it is highly desirable to engineer the atomic-level structures of 2D materials, such as introducing atomic-scale cation and/or anion vacancies, for achieving efficient kinetics of light-excited electrons/holes in photocatalysts.[32–38] These atomic-level defects with positive/negative charges can serve as the efficient trapping sites to temporarily accommodate the photo-generated electrons/holes only, thus achieving effective dissociation/migration of electron–hole pairs. It is interesting but also challenging to reveal the roles of these atomic-level defects for regulating the charge dynamics. Thus, using state-of-art characterizations to disclose the element/space/time-resolved electrons/holes dynamics in photocatalysts is desirable. More importantly, relating the above-disclosed charge kinetics with the atomic-scale structures/compositions in photocatalysts is pivotal to direct atomic-level design/fabrication of high-activity photocatalysts.

A. Talebian-Kiakalaieh, E. M. Hashem, M. Guo, B. Xia, J. Ran, S.-Z. Qiao
School of Chemical Engineering
University of Adelaide
Adelaide, SA 5005, Australia
E-mail: jingrun.ran@adelaide.edu.au; s.qiao@adelaide.edu.au

The ORCID identification number(s) for the author(s) of this article can be found under https://doi.org/10.1002/admt.202301213

**ADVANCED
SCIENCE NEWS**

www.advancedsciencenews.com

**ADVANCED
MATERIALS
TECHNOLOGIES**

www.advmattechnol.de

Unfortunately, this sort of research is also rarely covered in photocatalysis.

Herein, we for the first time design and fabricate the atomic-scale defected HfS$_2$ NSs using a sonication route. The as-fabricated atomic-scale defected HfS$_2$ NSs were coupled with four different photocatalysts to fabricate the new HfS$_2$-TiO$_2$, HfS$_2$-CdS, HfS$_2$-ZnIn$_2$S$_4$, and HfS$_2$-C$_3$N$_4$ composites, respectively. All four composites exhibit the apparent elevation of photocatalytic H$_2$ generation in triethanolamine (TEOA) aqueous solution, suggesting the universal enhancement effect by HfS$_2$ NSs for photocatalytic H$_2$ evolution. The highest photocatalytic H$_2$ evolution rate (5971 µmol g^{-1} h^{-1}) is observed on the optimized HfS$_2$-CdS. The optimized HfS$_2$-CdS also displays obviously-raised evolution rates of H$_2$ (2419 µmol g^{-1} h^{-1}) and benzaldehyde (5.11 mmol g^{-1} h^{-1}) in benzyl alcohol aqueous solution. Indeed, the obtained results strongly confirm the tremendous impact of the heterojunction photocatalytic systems, which have been adopted to accelerate the migration of photogenerated electrons and holes to various counterparts for reduction and oxidation reactions and to prolong their lifetimes.[39] Such phenomenon could be revealed by application of various in situ characterization analysis, such as in situ X-Ray photoelectron spectroscopy, in situ atomic force microscopy-Kelvin probe force microscopy, and ultrafast transient absorption spectroscopy. Actually, the atomic-scale S vacancies of HfS$_2$ NSs are found to temporarily attract photo-excited electrons, thus resulting in efficient spatiotemporal dissociation/migration of photo-excited electron–hole pairs in 40.0H. This Research demonstrates the great importance of developing distinctive 2D materials with atomic-scale defects for efficient solar-to-chemicals conversion.

2. Results and Discussion

2.1. Structures and Compositions

First, we synthesized HfS$_2$ nanosheets (NSs) via exfoliating bulk HfS$_2$ in ethanol using the sonication route in the ice bath. Then, the sonicated HfS$_2$ suspensions were centrifuged to remove the thick/large HfS$_2$ and acquire the thin/small HfS$_2$ NSs dispersed in ethanol. The X-ray diffraction (XRD) pattern of bulk HfS$_2$ (Figure S1, Supporting Information) exhibits the hexagonal phase HfS$_2$. The high-angle annular dark field-scanning transmission electron microscopy (HAADF-STEM) image (Figure S2a, Supporting Information) of bulk HfS$_2$ indicates the lattice spacing distances of 3.1 and 3.1 Å with an angle of 60°, corresponding to the (100) and (010) facet of hexagonal HfS$_2$. The atomic-resolution differential phase contrast (DPC)-STEM image (Figure S2b, Supporting Information) and corresponding line analysis of bulk HfS$_2$ (Figure S2c, Supporting Information) disclose the absence of any S vacancy in bulk HfS$_2$. The HAADF-STEM image of HfS$_2$ NSs (Figure S3a, Supporting Information) exhibits the 2D NSs morphology with the lateral sizes of ≈300–400 nm for HfS$_2$ NSs. The energy-dispersive X-Ray (EDX) spectroscopy of HfS$_2$ NSs in Figure S3b (Supporting Information) indicates the existence of Hf and S elements. Furthermore, the HAADF-STEM image (Figure S4a, Supporting Information) and corresponding elemental mapping images of Hf (Figure S4b, Supporting Information) and S (Figure S4c, Supporting Informa-

tion) for HfS$_2$ NSs further confirm the successful synthesis of HfS$_2$ NSs. Moreover, the AFM image (Figure S5a, Supporting Information) and corresponding height profile (Figure S5b, Supporting Information) reveal that the thickness of HfS$_2$ NSs is ≈30–40 nm. The atomic-resolution HAADF-STEM image (**Figure 1**a) shows the lattice distance values of 3.1 and 3.1 Å with an angle of 60°, corresponding to the (010) and (100) facets of hexagonal HfS$_2$. The Atomic-Resolution DPC-STEM image (Figure 1b) and corresponding line analyses (Figure 1c-e) together confirm the existence of S vacancies (V_S) in HfS$_2$ NSs. These results confirm the successful synthesis of atomic-scale defected HfS$_2$ NSs. These S vacancies can possibly enhance the interaction between HfS$_2$ NSs and photocatalyst loaded on the surface. Subsequently, CdS nanoparticles (NPs) were synthesized by a hydrothermal approach. The TEM image of as-synthesized CdS NPs (Figure S6a, Supporting Information), as abbreviated as 0.0H, shows the aggregation of CdS NPs with sizes of ≈10–30 nm. The high-resolution TEM (HRTEM) image (Figure S6b, Supporting Information) of 0.0H exhibits two lattice spacing values of 3.4 and 3.4 Å with an angle of 109.5°, corresponding to the (111) and (1-1-1) facets of cubic-phase CdS. The EDX spectrum of 0.0H in Figure S6c (Supporting Information) shows the existence of Cd and S elements. The HAADF-STEM image (Figure S6d, Supporting Information) and the corresponding elemental mapping images of Cd (Figure S6e, Supporting Information) and S (Figure S6f, Supporting Information) also confirm the successful synthesis of CdS NPs.[40] Subsequently, a range of HfS$_2$ coupled CdS (HfS$_2$/CdS) composite photocatalysts were fabricated by a simple physical mixing at room temperature. Specifically, 50 mg of the as-synthesized CdS NPs were combined with 20.0, 30.0, 40.0, and 50.0 mL of HfS$_2$ NSs ethanol solutions, respectively. The as-synthesized samples were labeled as 20.0H, 30.0H, 40.0H, and 50.0H, respectively. The XRD patterns of 0.0H and 40.0H are shown in Figure S7 (Supporting Information). No obvious change of the peak positions and intensities for CdS phase is found since the physical mixing of HfS$_2$ NSs and CdS NPs at room temperature can't affect the crystal structure of CdS phase. The existence of small XRD peaks assigned to HfS$_2$ phase is observed in the XRD pattern of 40.0H, also suggesting the combination of HfS$_2$ with CdS in 40.0H. TEM image of 40.0H (**Figure 2**a) indicates the dispersion of CdS NPs on the surface of HfS$_2$ NSs. High-Resolution HAADF-STEM image of 40.0H (Figure 2b) shows the lattice spacing values of 3.1 and 2.1 Å with an angle of 109.9°, ascribed to the (100) and (−112) facets of hexagonal HfS$_2$ NSs, respectively. Figure 2b also shows the lattice spacing values of 3.4 and 3.4 Å with an angle of 70.5°, attributed to the (111) and (11-1) planes of cubic CdS, respectively. The EDX spectrum (Figure 2c) further confirms the existence of Cd, S, and Hf elements for 40.0H. The HAADF-STEM image (Figure 2d) and the corresponding elemental mapping images of Hf, Cd, and S elements for 40.0H (Figure 2e-g) also confirm the successful loading of CdS NPs on surface of HfS$_2$ NSs. The high-resolution XPS spectra of 40.0H (Figure S8, Supporting Information) further confirm the successful combination of CdS NPs with HfS$_2$ NSs in 40.0H.

The microstructure and pore size distribution of 0.0H and 40.0H were also studied by the nitrogen (N$_2$) sorption analysis. The results in Figure S9 (Supporting Information) indicate the
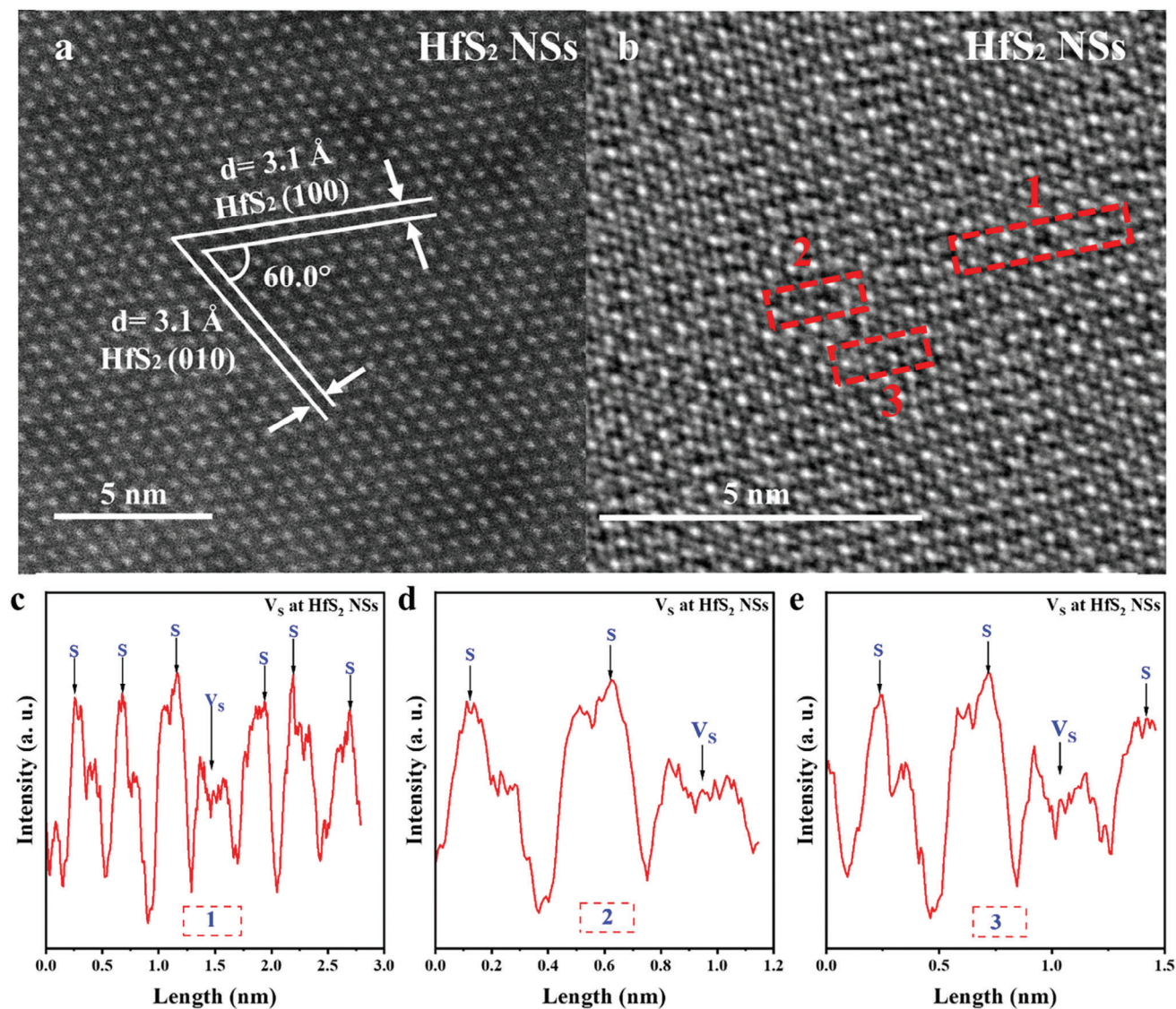
ADVANCED
SCIENCE NEWS
www.advancedsciencenews.com

ADVANCED
MATERIALS
TECHNOLOGIES
www.advmattechnol.de

Figure 1. a) Atomic-Resolution HAADF-STEM image, b) Atomic-Resolution DPC-STEM image, and c–e) corresponding line analyses for S vacancies in HfS$_2$ NSs.

overall down shift of the whole sorption isotherm for 40.0H, compared with that of 0.0H. Also, the pore size distribution curve of 40.0H is lower than that of 0.0H. Accordingly, Table S1 (Supporting Information) exhibits the reduced surface area (25.88 m^2 g^{-1}) and pore volume (0.155 cm^3 g^{-1}) of 40.0H, in contrast with those of 0.0H (50.00 m^2 g^{-1} and 0.284 cm^3 g^{-1}). This is because that the larger sizes of defected HfS$_2$ NSs (averaged thickness of ≈30–40 nm and lateral sizes of ≈300–400 nm) compared to those of CdS NPs (sizes of ≈10–30 nm) lead to lower surface areas and pore volumes arising from the stacking of the bigger-sized HfS$_2$ NSs.

2.2. Excellent Performances on H$_2$ and Benzaldehyde Evolution

The photocatalytic H$_2$ evolution activities of all the samples (0.0H, 20.0H, 30.0H, 40.0H, and 50.0H) were examined using

TEOA, benzyl alcohol (BA) and benzylamine as the substrates, respectively. As displayed in **Figure 3**a, 0.0H (bare CdS) only exhibits a photocatalytic H$_2$ evolution rate of 574 µmol g^{-1} h^{-1}, ascribing to rapid electron–hole recombination. In contrast, all the HfS$_2$/CdS composites (20.0H, 30.0H, 40.0H, and 50.0H) exhibit obviously-raised photocatalytic H$_2$ evolution rates of 1034, 2316, 5971, and 2394 µmol g^{-1} h^{-1}, respectively, compared to CdS alone. Especially, 40.0H exhibits the highest photocatalytic H$_2$ evolution rate of 5971 µmol g^{-1} h^{-1}, due to the excellent balance of charge kinetics and light harvesting. Since 40.0H exhibits the highest photocatalytic H$_2$ evolution rate of 5971 µmol g^{-1} h^{-1}, we further tested the photocatalytic H$_2$ evolution rates of 40.0H using BA and benzylamine as the substrates, respectively. As shown in Figure 3b, 40.0H shows the obviously-raised photocatalytic H$_2$ evolution rates of 2419 and 2452 µmol g^{-1} h^{-1} in BA and benzylamine aqueous solution, respectively. In contrast, 0.0H only exhibits the photocatalytic H$_2$ evolution rates
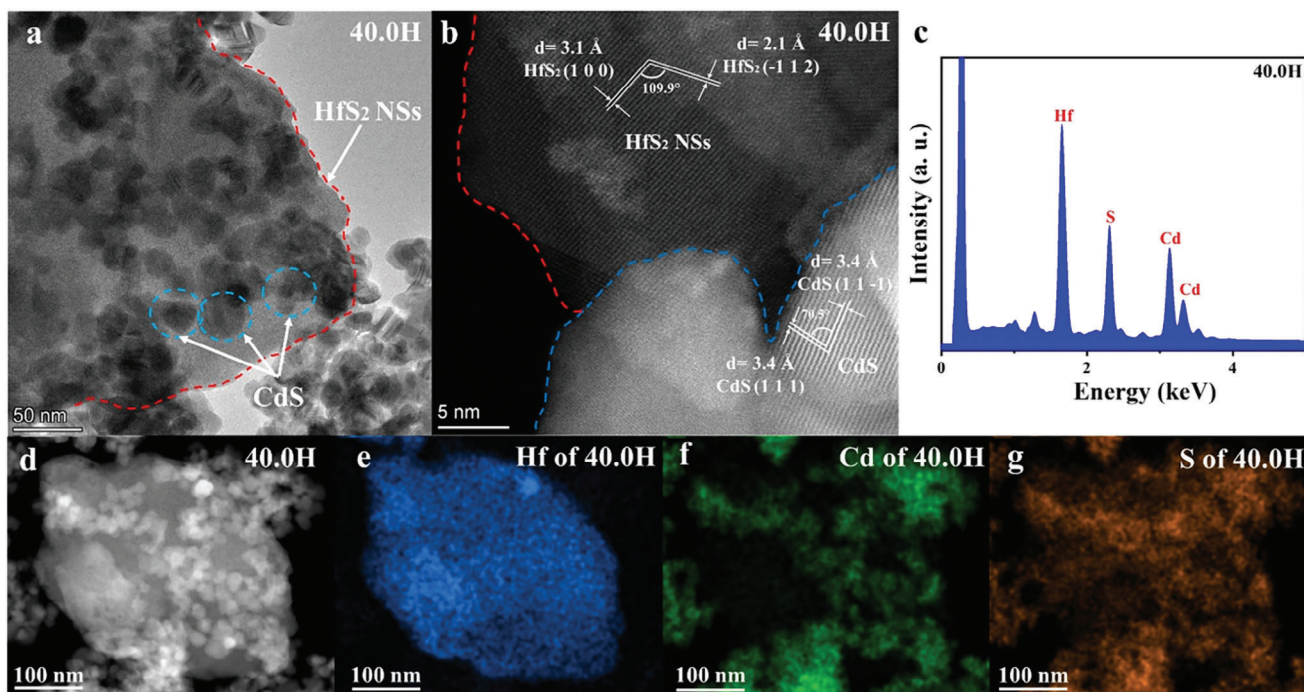
Figure 2. a) TEM image, b) high-resolution HAADF-STEM image, and c) EDX spectrum of 40.0H. d) HAADF-STEM image and the corresponding elemental mapping images of e) Hf, f) Cd, and g) S elements for 40.0H.

of 957 and 983 µmol g^{-1} h^{-1} in BA and benzylamine aqueous solution, respectively. These results show the enhancement factors of ≈253% and ≈249% in H_2 evolution rates for 40.0H in BA and benzylamine aqueous solution, respectively. H_2 evolution rate of 40.0H was compared with reported studies and the results are reported in Table S2 (Supporting Information). Our work shows one of the highest photocatalytic H_2 evolution rates, suggesting excellent photocatalytic performance for 40.0H. Furthermore, 40.0H exhibits the photocatalytic H_2 evolution rates of 607 and 481 µmol g^{-1} h^{-1} using 365 and 420 nm light emitting diode (LED) irradiation, respectively (Figure S10, Supporting Information). In addition, photocatalytic H_2 evolution over HfS_2 NSs was investigated in various reaction conditions. As shown in Figure 3b, HfS_2 NSs exhibit the low photocatalytic H_2 evolution activities in TEOA, BA, and benzylamine aqueous solution, respectively. Thus, HfS_2 NSs only contribute to a small section in the photocatalytic activities of 40.0H in various reaction conditions (Figure 3b). Furthermore, the stability of photocatalytic H_2 evolution on 40.0H was also tested. It can be observed that 40.0H reserves the excellent stability for photocatalytic H_2 evolution in 12 h reaction (Figure S11, Supporting Information). Interestingly, compared to H_2 evolution amounts in the first cycle, the H_2 evolution amounts decrease in the second and third cycles, but increase again in the fourth cycle. These slight changes of H_2 evolution arises from several possible factors, such as environmental temperature, agglomeration of photocatalyst in reactor, and effective interaction between HfS_2 NSs and CdS NPs in reactor. The reacted 40.0H (annotated as 40.0H-R), shows no obvious difference in the morphology (Figure S12a–c, Supporting Information) and chemical compositions (Figure S12d, Supporting Information) compared to those before the reaction (Figure 2a,c).

On the other hand, the photocatalytic benzaldehyde (BAD) evolution rates on 0.0H and 40.0H were also studied. As displayed in Figure S13a,b (Supporting Information), 0.0H exhibits the conversion of 49.70% and selectivity of 14.31% in 12 h reaction, leading to the averaged BAD evolution rate of 3.32 mmol g^{-1} h^{-1}. As a contrast, 40.0H shows the conversion of 54.61% and selectivity of 20.04% in 12 h reaction, corresponding to the averaged BAD evolution rate of 5.11 mmol g^{-1} h^{-1}. Therefore, 40.0H exhibits ≈154% times higher averaged BAD evolution rate in 12 h reaction, compared with that of 0.0H. All these results confirm the obvious rise on photocatalytic co-generation of H_2 and BAD for 40.0H, compared to those of 0.0H. Additionally, the possible by-products are benzoic acid and benzyl benzoate.[41–43]

2.3. Light Absorption and Band Structures

To investigate the reason on the simultaneous raises on H_2 and BAD evolution of 40.0H, various advanced characterizations were adopted to study the light absorption, charge kinetics, and surface redox reactions of 40.0H. First, we used UV–vis diffuse reflectance spectroscopy to explore the light absorption properties of 0.0H, 40.0H, HfS_2 NSs, and bulk HfS_2. The colors of these samples are shown in Figure S14 (Supporting Information). The corresponding results (Figure S14, Supporting Information) exhibit that the absorption edge is red-shifted from 558.6 nm for 0.0H to 574.3 nm for 40.0H. This indicates the increased light responsive range for 40.0H compared to that of 0.0H, due to the introduction of HfS_2 NSs with a much smaller bandgap (1.42 eV) than that of CdS (2.22 eV). After the combination with HfS_2 NSs, 40.0H shows an obviously reduced light absorption in the
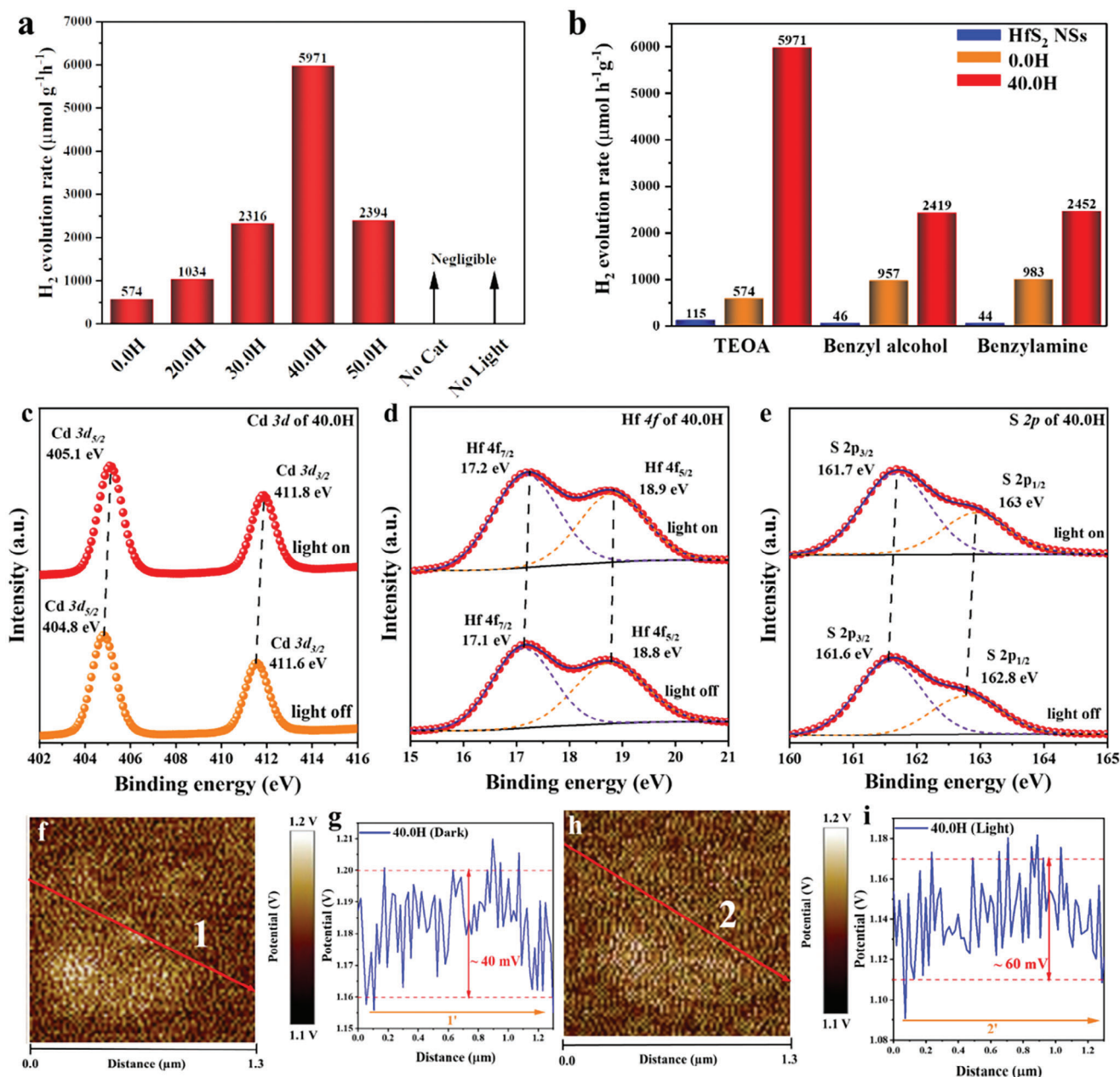
**ADVANCED
SCIENCE NEWS**

www.advancedsciencenews.com

**ADVANCED
MATERIALS
TECHNOLOGIES**

www.advmattechnol.de

Figure 3. a) Photocatalytic H$_2$ evolution rates of 0.0H, 20.0H, 30.0H, 40.0H, and 50.0H in ≈17 vol.% triethanolamine aqueous solution using xenon light (λ >400 nm). The results on blank experiments in the absence of catalyst and light, respectively, are shown. Notably, in the blank experiments, all the other conditions remain the same. b) Photocatalytic H$_2$ evolution rates of HfS$_2$ NSs, 0.0H, and 40.0H in ≈17 vol.% triethanolamine aqueous solution, BA aqueous solution, and benzylamine aqueous solution, respectively, using xenon light (λ >400 nm). c) High-Resolution XPS spectra of Cd 3d for 40.0H with light on and off, respectively. d) High-Resolution XPS spectra of Hf 4f for 40.0H with light on and off, respectively. e) High-Resolution XPS spectra of S 2p for 40.0H with light on and off, respectively. f) KPFM image of 40.0H in darkness. g) The corresponding line analysis of potential signal for 40.0H in darkness along line 1 (Figure 3g). h) KPFM image of 40.0H with light illumination. i) The corresponding line analysis of potential signal for 40.0H with light illumination along line 2 (same line; Figure 3h).

range of 250–≈550 nm and raised light absorption in the range of ≈550–800 nm, compared with 0.0H. This difference arises from the much lower light absorption in the range of 250–≈550 nm and higher light absorption in the range of ≈550–800 nm for 40.0H, compared with that of 0.0H. Thus, we need to confirm whether the enhanced light absorption in the range of ≈550–

800 nm can help raise the photocatalytic activity of 40.0H. 740-nm LED instead of xenon light was utilized to test the photocatalytic H$_2$ evolution activity of 40.0H (Figure S15, Supporting Information). No activity was observed in the above conditions, suggesting the enhanced light absorption at ≈550–800 nm probably imposes no effect on the activity for 40.0H.

**ADVANCED
SCIENCE NEWS**

www.advancedsciencenews.com

**ADVANCED
MATERIALS
TECHNOLOGIES**

www.advmattechnol.de

Then, the band structures of HfS_2 NSs and CdS (0.0H) were calculated, respectively. Figure S16a (Supporting Information) exhibits the Mott-Schottky (M–S) plot of HfS_2 NSs, suggesting its flat band potential of +0.76 V versus Ag/AgCl electrode. Thus, the Fermi level of HfS_2 NSs is +0.76 V versus Ag/AgCl electrode, corresponding to +1.36 V versus the Reversible hydrogen electrode (RHE). The XPS valence band (VB) spectrum of HfS_2 NSs is 0.41 eV (Figure S16b, Supporting Information). Thus, the VB position of HfS_2 NSs is +1.77 V versus RHE. According to the UV–vis diffuse reflectance spectrum of HfS_2 NSs (Figure S16c, Supporting Information), the bandgap of HfS_2 NSs is 1.42 eV. Thus, the CB position of HfS_2 NSs is calculated to be +0.35 V versus RHE. Thus, the CB and VB edge positions of HfS_2 NSs are shown in Figure S16d (Supporting Information). Then, we use the above same route to determine that the CB and VB edge positions of CdS (0.0H) are −1.03 and +1.19 V versus RHE, as shown in Figure S17a–d (Supporting Information). Thus, based on the band structures of HfS_2 NSs and CdS, a type II (straddling type) heterojunction is formed between HfS_2 NSs and CdS in 40.0H (Figure S18, Supporting Information).

2.4. Photo-Generated Electrons/Holes Kinetics

Photo-generated electrons/holes kinetics of 40.0H were studied using various types of characterizations including transient photocurrent (TPC) density measurement, steady-state photoluminescence (PL), in situ XPS, in situ AFM-Kelvin probe force microscopy (KPFM), steady-state/transient-state surface photovoltage (SPV) spectroscopy and ultrafast transient absorption spectroscopy (TAS). The TPC density measurements of 0.0H, 40.0H, and HfS_2 NSs are shown in Figure S19 (Supporting Information). HfS_2 NSs exhibit a very small TPC density value of ≈2.8 µA with light on, suggesting its low separation/transfer efficiency, probably arising from its intrinsic features. In comparison, bare CdS (0.0H) shows a much higher TPC density value of ≈9.6 µA with light on, followed by gradual reduction to ≈6.1 µA cm^{-2} within 60 s. These results indicate the better separation/transfer efficiency of CdS (0.0H) compared to that of HfS_2 NSs. As a comparison, 40.0H shows a higher TPC density of ≈10.0 µA cm^{-2} with light on, accompanied with a small reduction (≈1 µA cm^{-2}) on TPC density in 60 s. These results confirm the key role of HfS_2 NSs on effectively reducing the electron–hole recombination for 40.0H. Then, the steady-state PL spectra (Figure S20, Supporting Information) of 40.0H show the reduced PL peak intensity at ≈549 nm, compared with that of 0.0H at ≈559 nm, indicating the suppressed radiative electron–hole recombination in CdS phase of 0.0H and 40.0H. Compared with 0.0H, the tiny blue shift of PL peak observed for 40.0H is attributed to the slightly-raised bandgap width of CdS NPs, arising from the higher dispersion and less aggregation of CdS NPs on HfS_2 NSs than CdS NPs alone.[44] Furthermore, in situ, XPS were conducted with light on to provide the steady-state and element-resolved photo-generated electrons/holes separation/transfer information on 40.0H. As shown in Figure 3c–e, with light illumination, Cd 3d, Hf 4f, and S 2p peaks of 40.0H all shift to the higher binding energy direction, compared to those of 40.0H with light off. These results indicate the accumulation of more photo-generated holes than electrons on the surface of 40.0H (elements Cd, Hf, and S)

with light on. Then, in situ, AFM-Kelvin probe force microscopy (KPFM) with light illumination was performed to provide the steady-state and space-resolved photo-generated electrons/holes dissociation/migration on 40.0H. Figure S21a (Supporting Information) shows the dispersion of CdS NPs on the surface of HfS_2 NSs in darkness. This is further confirmed by the corresponding height profile (Figure S21b, Supporting Information) of 40.0H. Almost the same results (Figure S21c,d, Supporting Information) for 40.0H with light illumination are observed. The KPFM images and corresponding line analyses in the same region for 40.0H with light off and on are displayed in Figure 3f–i. As displayed in Figure 3g, without light illumination, 40.0H exhibits a potential difference of ≈40 mV between the highest potential point and the base. In contrast, a potential difference of ≈60 mV between the highest potential point and the base is observed for 40.0H with light illumination, suggesting the accumulation of more photo-generated holes than electrons on the surface of 40.0H with light illumination.[45,46] Then, we utilize the transient-state/steady-state SPV spectroscopy to study the dissociation/transfer/trapping/recombination of photo-excited electrons and holes on the surface of 0.0H and 40.0H (**Figure 4**a,b). As displayed in Figure 4a, 0.0H first exhibits a sharp rise to the highest positive SPV signal (≈17.66 µV) at ≈0.111 µs, suggesting the transfer of much more photo-excited holes than electrons on the surface of 0.0H at ≈0.111 µs. Then, we observe a rapid decay of the SPV positive signal to zero at ≈0.164 µs, suggesting that these photo-excited holes are rapidly recombining with the photo-excited electrons transferring to the surface of 0.0H. Subsequently, the SPV signal turns into negative and reaches the largest negative signal of ≈−22.73 µV at ≈7.424 µs, suggesting the gradual migration and accumulation of photo-excited electrons from bulk onto surface of 0.0H. The slower migration of photo-excited electrons than holes from bulk to the surface of 0.0H could be attributed to the existence of electron-trapping sites in the bulk of 0.0H. Then, we observe the gradual decay of the negative SPV signal to zero at ≈0.733 ms, due to the recombination of photo-excited electrons and holes on the surface of 0.0H. In contrast, after HfS_2 NSs combined with CdS NPs in 40.0H, a less steep spike is observed for 40.0H after light excitation, suggesting the slower transfer of photo-excited holes from bulk to surface. And also a lower highest SPV positive signal of ≈10.56 µV is achieved at ≈0.119 µs by 40.0H, followed by a much slower decay of the positive SPV signal to 0 at ≈10.62 µs. Then, the SPV signal turns negative and reaches the largest negative potential of ≈−5.37 µV at ≈122.79 µs. Finally, the negative SPV signal of 40.0H decays to zero at ≈1.845 ms. These results confirm that the introduction of HfS_2 NSs significantly extends the lifetime of photo-generated holes on the surface of 40.0H. Besides, the lifetime of photo-generated electrons in 40.0H is also elongated to some extent. However, the maximum numbers of photo-generated electrons and holes on the surface of 40.0H are reduced compared to those of 0.0H, as revealed by the lower largest negative/positive potentials of 40.0H than those of 0.0H (Figure 4a). This is further confirmed by the lower steady-state SPV value of 40.0H, in contrast with that of 0.0H (Figure 4b). Besides, the absolute transient-state SPV value of 40.0H is also lower than that of 0.0H (Figure 4a). The reason is that HfS_2 NSs to some extent block the light absorption by CdS NPs in 40.0H. Furthermore, ultrafast TAS was utilized to study
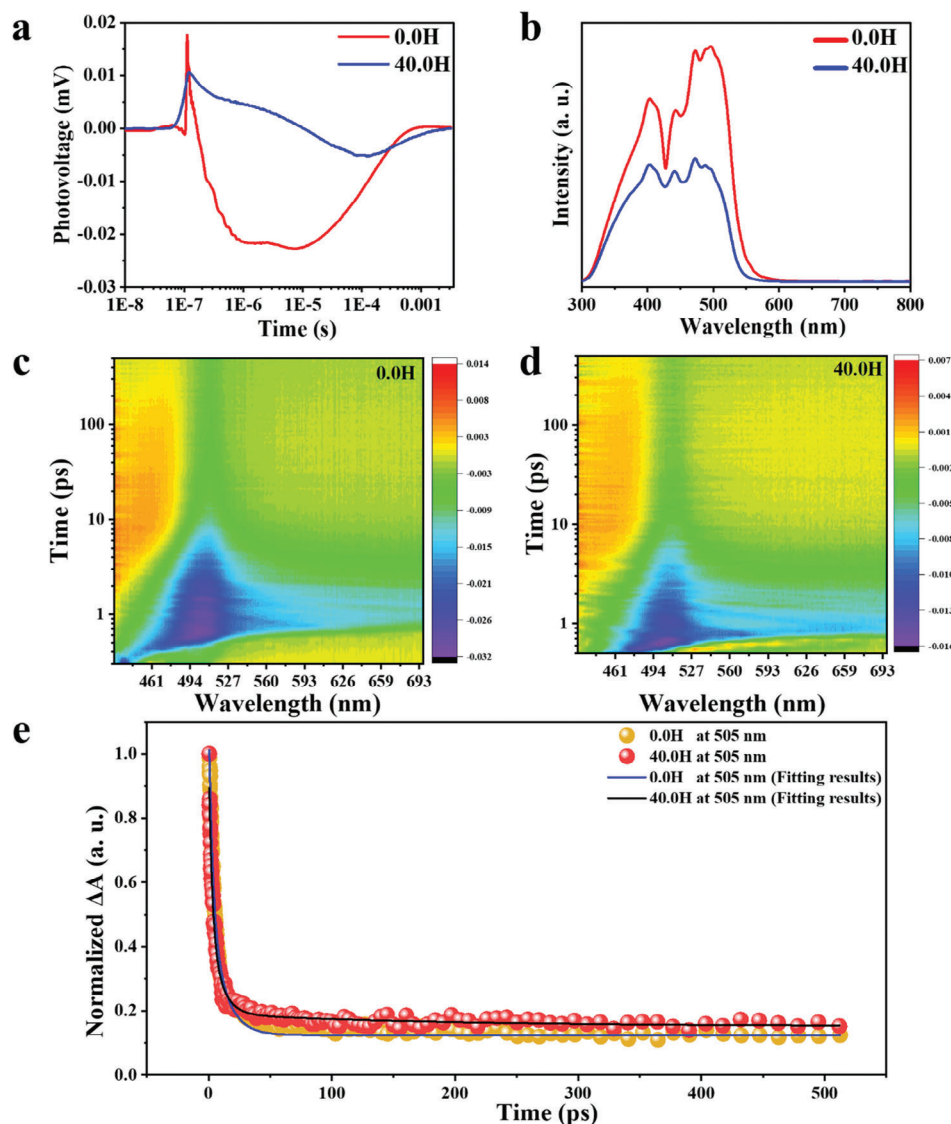
Figure 4. a) Transient-state SPV spectra of 0.0H and 40.0H. b) steady-state SPV spectra of 0.0H and 40.0H. 2D pseudo-color TA spectra of c) 0.0H and d) 40.0H after the excitation with a 400 nm laser pulse. e) Normalized decay kinetics and fitting lines for 0.0H and 40.0H taken through the GSB peaks at ≈505 nm.

the photo-generated charge carrier kinetics in 40.0H. As shown in Figure 4c,d, 2D pseudo-color TA spectra shows an obvious negative absorption in the range of ≈450–≈580 nm, attributed to the ground state bleaching (GSB) signal.[47,48] The normalized decay kinetics and corresponding fitting at 505 nm for 0.0H and 40.0H (Figure 4e) further demonstrate the slower decay of GSB signal for 40.0H, compared with that of 0.0H. Since GSB signal at 505 nm is directly related with the photo-excited holes in the VB of CdS phase in 0.0H and 40.0H, the slower decay kinetics of GSB signal indicates the longer lifetimes of photo-excited holes in CdS phase of 40.0H, in contrast with those of 0.0H. These results are in accordance with the above TPC density measurement (Figure S19, Supporting Information) and transient-state SPV results (Figure 4a). Therefore, according to the above results on TPC density measurement, steady-state PL, in situ XPS, in situ AFM-KPFM, steady-state/transient-state SPV, and ultrafast

TAS, we can conclude several things below: i) with HfS_2 NSs introduced in 40.0H, more photo-generated holes than electrons are driven to the surface of 40.0H with light illumination; ii) the lifetimes of both photo-generated electrons and holes (especially the hole lifetime) for 40.0H are elongated compared to those for 0.0H; iii) the maximum numbers of photo-generated electrons and holes on the surface of 40.0H are reduced to some extent, in contrast with those of 0.0H.

2.5. Surface Redox Reactions and Photocatalytic Mechanism

Finally, we studied the surface redox reactions on 40.0H, which are H_2 evolution and BA oxidation reactions, respectively. As displayed in Figure S22 (Supporting Information), after introducing HfS_2 NSs, no obvious change on the overpotential for H_2

**ADVANCED
SCIENCE NEWS**

www.advancedsciencenews.com

**ADVANCED
MATERIALS
TECHNOLOGIES**

www.advmattechnol.de

evolution is observed for 40.0H, compared to that of 0.0H. These results suggest that HfS$_2$ NS is not an excellent H$_2$ evolution catalysts. Thus, HfS$_2$ NSs in 40.0H don't serve as the co-catalyst like Pt or MoS$_2$ reported in the references. Instead, HfS$_2$ NSs could function as the key component in type II hetero-junction (Figure S18, Supporting Information) to raise the photocatalytic performance of 40.0H. For the BA oxidation reaction, the 12 h BA conversion (54.61%) and BAD selectivity (20.04%) for 40.0H are obviously higher than those of 0.0H (BA conversion: 49.70%; BAD selectivity: 14.31%) as shown in Figure S13a,b (Supporting Information). These results indicate that the introduction of HfS$_2$ NSs not only raises the oxidative conversion of BA, but also increases the selectivity of BA-to-BAD transformation. Based on the above results, the photocatalytic mechanisms of H$_2$ and BAD evolution on 40.0H is raised in Figure S23 (Supporting Information). With light illumination, photo-excited electrons and holes are generated in the CB and VB of CdS and HfS$_2$, respectively. Then, since CdS and HfS$_2$ are combined together to form the type II heterojunction, the photo-generated electrons are transferred from the CB of CdS to the CB of HfS$_2$ for H$_2$ evolution; whilst the photo-generated holes are transferred from the VB of HfS$_2$ to the VB of CdS for the oxidation of BA to form BAD. This type II heterojunction raises the efficiency of photo-generated electron/hole dissociation/transfer in 40.0H, compared to 0.0H. Besides, due to the existence of atomic-level S vacancies in HfS$_2$ NSs, the photo-generated electrons transferred to the CB of HfS$_2$ NSs are temporarily trapped by the atomic-level S vacancies, thus retarding the recombination of electrons with holes in HfS$_2$ NSs. Then, these photo-generated electrons will be released to reduce protons and forming H$_2$ gas. Thus, these atomic-scale S vacancies in HfS$_2$ NSs further raise the photocatalytic performance of 40.0H via

realizing the spatiotemporal separation of electrons and holes. Thus, the roles of HfS$_2$ NS in 40.0H are summarized as follows: i) it serves as the platform to boost the general dispersion and intimate contact of CdS NPs; ii) the formation of type II heterojunction between HfS$_2$ NSs and CdS NPs boosts the efficient charge separation/transfer; iii) the atomic-scale S vacancies in HfS$_2$ NSs function as the electron trap to reduce the electron–hole recombination.

2.6. HfS$_2$ NSs Raising Activities on ZnIn$_2$S$_4$, C$_3$N$_4$, and TiO$_2$

To confirm that HfS$_2$ NSs can raise the photocatalytic H$_2$ evolution of various photocatalysts, we have for the first time synthesized a range of HfS$_2$-based photocatalysts including HfS$_2$-TiO$_2$, HfS$_2$-ZnIn$_2$S$_4$, and HfS$_2$-C$_3$N$_4$ using the similar method for fabricating 40.0H. They are labeled as 40HfS$_2$-TiO$_2$, 40HfS$_2$-ZnIn$_2$S$_4$, and 40HfS$_2$-C$_3$N$_4$, respectively. The XRD patterns of TiO$_2$, 40HfS$_2$-TiO$_2$, ZnIn$_2$S$_4$, 40HfS$_2$-ZnIn$_2$S$_4$, C$_3$N$_4$ and 40HfS$_2$-C$_3$N$_4$ are displayed in **Figure 5**a-c. Several new peaks ascribed to HfS$_2$ are observed for 40HfS$_2$-TiO$_2$, 40HfS$_2$-ZnIn$_2$S$_4$, and 40HfS$_2$-C$_3$N$_4$, confirming the successful combination of HfS$_2$ NSs with TiO$_2$, ZnIn$_2$S$_4$, and C$_3$N$_4$, respectively. Besides, no apparent change for the positions and intensities of diffraction peaks for TiO$_2$ in 40HfS$_2$-TiO$_2$, ZnIn$_2$S$_4$ in 40HfS$_2$-ZnIn$_2$S$_4$, and C$_3$N$_4$ in 40HfS$_2$-C$_3$N$_4$ are observed, compared to TiO$_2$, ZnIn$_2$S$_4$, and C$_3$N$_4$, respectively. Furthermore, the TEM images

(Figure S24a,c,e, Supporting Information) and the corresponding EDX spectra (Figure S24b,d,f, Supporting Information) of 40HfS$_2$-TiO$_2$, 40HfS$_2$-ZnIn$_2$S$_4$, and 40HfS$_2$-C$_3$N$_4$ further corroborate the coupling of HfS$_2$ NSs with TiO$_2$, ZnIn$_2$S$_4$, and C$_3$N$_4$, respectively. Then, the photocatalytic H$_2$ evolution of 40HfS$_2$-TiO$_2$, 40HfS$_2$-ZnIn$_2$S$_4$, and 40HfS$_2$-C$_3$N$_4$ were tested in ≈17 vol.% triethanolamine aqueous solution using xenon light. As shown in Figure 5d, compared with TiO$_2$, ZnIn$_2$S$_4$, or C$_3$N$_4$ alone, 40HfS$_2$-TiO$_2$, 40HfS$_2$-ZnIn$_2$S$_4$, or 40HfS$_2$-C$_3$N$_4$ exhibit the apparently-raised photocatalytic H$_2$ evolution rates, suggesting that HfS$_2$ NSs can raise the H$_2$ evolution of these photocatalysts. These results further confirm that HfS$_2$ NSs can serve as an excellent platform to universally raise the photocatalytic H$_2$ evolution on various photocatalysts. To investigate the reasons on the raised photocatalytic efficiency, both the light absorption properties and charge recombination of these photocatalysts were studied. First, UV–vis diffuse reflectance spectroscopy was adopted to study the light-harvesting abilities of the as-synthesized photocatalysts. As displayed in Figure S25a–c (Supporting Information), obviously raised light absorption in the range of ≈500–800 nm was observed for 40HfS$_2$-TiO$_2$, 40HfS$_2$-ZnIn$_2$S$_4$, and 40HfS$_2$-C$_3$N$_4$, due to the existence of HfS$_2$ NSs. Furthermore, steady-state PL spectra (Figure S26a–c, Supporting Information) indicate the reduced steady-state PL intensities of 40HfS$_2$-TiO$_2$, 40HfS$_2$-ZnIn$_2$S$_4$, and 40HfS$_2$-C$_3$N$_4$, compared with those of TiO$_2$, ZnIn$_2$S$_4$, and C$_3$N$_4$, respectively. These results indicate the impeded charge recombination in 40HfS$_2$-TiO$_2$, 40HfS$_2$-ZnIn$_2$S$_4$, and 40HfS$_2$-C$_3$N$_4$ due to the introduction of HfS$_2$ NSs. The above results on TEM images, steady-state PL spectra, and photocatalytic activities together confirm the successful establishment of effective and intimate junction between HfS$_2$ NSs with TiO$_2$, ZnIn$_2$S$_4$, and C$_3$N$_4$, respectively. These effective junctions in 40HfS$_2$-TiO$_2$, 40HfS$_2$-ZnIn$_2$S$_4$, and 40HfS$_2$-C$_3$N$_4$ also enable that HfS$_2$ NSs could serve as a universal platform to significantly raise the photocatalytic activities. Especially, the atomic-scale S vacancies in HfS$_2$ NSs work as the electron trap to boost the electron–hole separation/transfer.

3. Conclusion

In conclusion, we fabricated the novel HfS$_2$ nanosheets (NSs) with atomic-scale S vacancies via the sonication route. Thus, the as-synthesized HfS$_2$ NSs were combined with different photocatalysts to acquire the new HfS$_2$-TiO$_2$, HfS$_2$-CdS, HfS$_2$-ZnIn$_2$S$_4$, and HfS$_2$-C$_3$N$_4$ composite photocatalysts, respectively. Among them, optimized HfS$_2$-CdS composite displays the largest photocatalytic H$_2$ evolution rate (5971 µmol g^{-1} h^{-1}) in triethanolamine aqueous solution, together with evidently raised generation activities of H$_2$ (2419 µmol g^{-1} h^{-1}) and benzaldehyde (5.11 mmol g^{-1} h^{-1}) than bare CdS in benzyl alcohol aqueous solution. Advanced characterizations, such as in situ X-ray photoelectron spectroscopy (XPS), in situ atomic force microscopy-Kelvin probe force microscopy (AFM-KPFM) and ultrafast transient absorption spectroscopy (TAS), together reveal that the numerous atomic-level S vacancies in HfS$_2$ NSs function as the trapping centers to temporarily host the electrons, thus significantly boosting the electron–hole separation/transfer in 40.0H. Our work not only demonstrates the significance of atomic-scale regulation on new 2D materials for photocatalysis application, but also
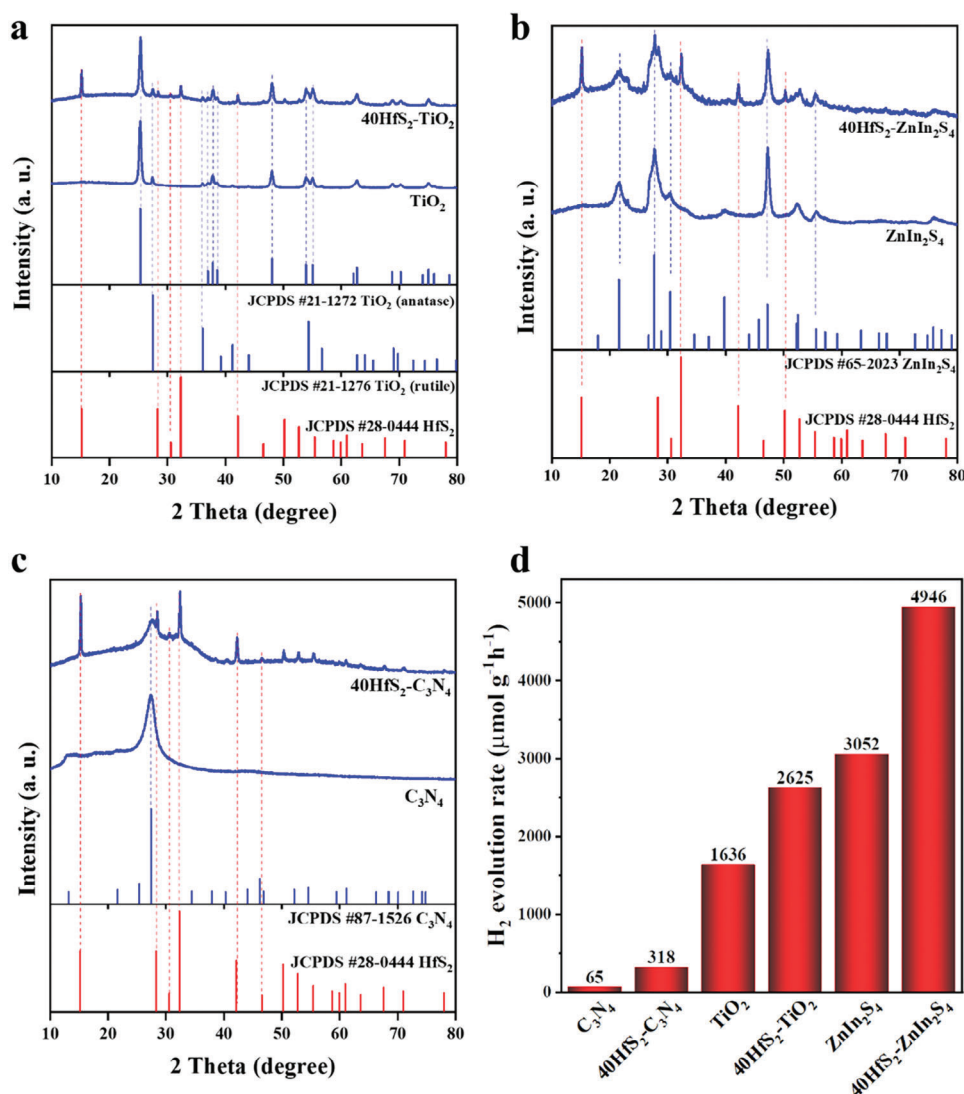
**ADVANCED
SCIENCE NEWS**

www.advancedsciencenews.com

**ADVANCED
MATERIALS
TECHNOLOGIES**

www.advmattechnol.de

Figure 5. XRD patterns of a) TiO_2 and $40HfS_2$-TiO_2, b) $ZnIn_2S_4$, and $40HfS_2$-$ZnIn_2S_4$, c) C_3N_4 and $40HfS_2$-C_3N_4, and d) Photocatalytic H_2 evolution rates of C_3N_4, $40HfS_2$-C_3N_4, TiO_2, $40HfS_2$-TiO_2, $ZnIn_2S_4$ and $40HfS_2$-$ZnIn_2S_4$ in ≈17 vol.% triethanolamine aqueous solution.

highlights the importance of using state-of-art characterizations to investigate the elements/space/time-resolved electrons/holes dynamics of photocatalysts.

4. Experimental Section

Experimental details can be found in the Supporting Information.

Supporting Information

Supporting Information is available from the Wiley Online Library or from the author.

Conflict of Interest

The authors declare no conflict of interest.

Data Availability Statement

The data that support the findings of this study are available from the corresponding author upon reasonable request.

**ADVANCED
SCIENCE NEWS**

www.advancedsciencenews.com

**ADVANCED
MATERIALS
TECHNOLOGIES**

www.advmattechnol.de

[1] Z. Teng, Q. Zhang, H. Yang, K. Kato, W. Yang, Y. Lu, S. Liu, C. Wang, A. Yamakata, C. Su, B. Liu, T. Ohno, *Nat. Catal.* **2021**, *4*, 374.

[2] H. Nishiyama, T. Yamada, M. Nakabayashi, Y. Maehara, M. Yamaguchi, Y. Kuromiya, Y. Nagatsuma, H. Tokudome, S. Akiyama, T. Watanabe, R. Narushima, S. Okunaka, N. Shibata, T. Takata, T. Hisatomi, K. Domen, *Nature* **2021**, *598*, 304.

[3] W. Zhao, P. Yan, B. Li, M. Bahri, L. Liu, X. Zhou, R. Clowes, N. D. Browning, Y. Wu, J. W. Ward, A. I. Cooper, *J. Am. Chem. Soc.* **2022**, *144*, 9902.

[4] M. Kou, Y. Wang, Y. Xu, L. Ye, Y. Huang, B. Jia, H. Li, J. Ren, Y. Deng, J. Chen, Y. Zhou, K. Lei, L. Wang, W. Liu, H. Huang, T. Ma, *Angew. Chem., Int. Ed.* **2022**, *61*, e202200413.

[5] H. Song, S. Luo, H. Huang, B. Deng, J. Ye, *ACS Energy Lett.* **2022**, *7*, 1043.

[6] L. Capaldo, D. Ravelli, M. Fagnoni, *Chem. Rev.* **2022**, *122*, 1875.

[7] Y. Hou, A. B. Laursen, J. Zhang, G. Zhang, Y. Zhu, X. Wang, S. Dahl, I. Chorkendorff, *Angew. Chem., Int. Ed.* **2013**, *52*, 3621.

[8] J. Hong, Y. Wang, Y. Wang, W. Zhang, R. Xu, *ChemSusChem* **2013**, *6*, 2263.

[9] S. Martha, A. Nashim, K. M. Parida, *J Mater Chem* **2013**, *1*, 7816.

[10] K. Iwashina, A. Iwase, Y. H. Ng, R. Amal, A. Kudo, *J. Am. Chem. Soc.* **2015**, *137*, 604.

[11] G. Zuo, Y. Wang, W. L. Teo, A. Xie, Y. Guo, Y. Dai, W. Zhou, D. Jana, Q. Xian, W. Dong, Y. Zhao, *Angew. Chem., Int. Ed.* **2020**, *59*, 11287.

[12] R. Yang, Y. Fan, Y. Zhang, L. Mei, R. Zhu, J. Qin, J. Hu, Z. Chen, Y. Hau Ng, D. Voiry, S. Li, Q. Lu, Q. Wang, J. C. Yu, Z. Zeng, *Angew. Chem., Int. Ed.* **2023**, *62*, e202218016.

[13] L. Sun, Z. Zhao, S. Li, Y. Su, L. Huang, N. Shao, F. Liu, Y. Bu, H. Zhang, Z. Zhang, *ACS Appl. Nano Mater.* **2019**, *2*, 2144.

[14] K. Chen, H. Guo, J. Zhang, L. Wang, M. Wu, *ACS Appl. Energy Mater.* **2022**, *5*, 10657.

[15] Q. Lu, Y. Yu, Q. Ma, B. Chen, H. Zhang, *Adv. Mater.* **2016**, *28*, 1917.

[16] X. Dang, X. Xie, F. Dai, J. Guo, J. Liu, X. Lu, *Adv. Mater. Interfaces* **2021**, *8*, 2100151.

[17] Y. Jin, D. Jiang, D. Li, P. Xiao, X. Ma, M. Chen, *ACS Sustainable Chem. Eng.* **2017**, *5*, 9749.

[18] B. Lin, Z. Chen, P. Song, H. Liu, L. Kang, J. Di, X. Luo, L. Chen, C. Xue, B. Ma, G. Yang, J. Tang, J. Zhou, Z. Liu, F. Liu, *Small* **2020**, *16*, 2003302.

[19] J. Shi, S. Li, F. Wang, L. Gao, Y. Li, X. Zhang, J. Lu, *Dalton Trans.* **2019**, *48*, 3327.

[20] S. Liu, K. Wang, M. Yang, Z. Jin, *Acta Phys. Chim. Sin.* **2022**, *38*, 2109023.

[21] Y.-J. Yuan, D. Chen, Z.-T. Yu, Z.-G. Zou, *J Mater Chem* **2018**, *6*, 11606.

[22] J. Jia, W. Sun, Q. Zhang, X. Zhang, X. Hu, E. Liu, J. Fan, *Appl. Catal., B* **2020**, *261*, 118249.

[23] H.-T. Fan, Z. Wu, K.-C. Liu, W.-S. Liu, *Chem. Eng. J.* **2022**, *433*, 134474.

[24] R. Xiao, C. Zhao, Z. Zou, Z. Chen, L. Tian, H. Xu, H. Tang, Q. Liu, Z. Lin, X. Yang, *Appl. Catal., B* **2020**, *268*, 118382.

[25] T. Yang, Y. Shao, J. Hu, J. Qu, X. Yang, F. Yang, C. Ming Li, *Chem. Eng. J.* **2022**, *448*, 137613.

[26] D. Kim, K. Yong, *Appl. Catal., B* **2021**, *282*, 119538.

[27] Y. Qin, H. Li, J. Lu, Y. Feng, F. Meng, C. Ma, Y. Yan, M. Meng, *Appl. Catal., B* **2020**, *277*, 119254.

[28] J. Ye, K. Liao, X. Ge, Z. Wang, Y. Wang, M. Peng, T. He, P. Wu, H. Wang, Y. Chen, Z. Cui, Y. Gu, H. Xu, T. Xu, Q. Li, X. Zhou, M. Luo, N. Li, M. Zubair, F. Wu, P. Wang, C. Shan, G. Wang, J. Miao, W. Hu, *Adv. Opt. Mater.* **2021**, *9*, 2002248.

[29] Y. Bai, H. Zhang, X. Wu, N. Xu, Q. Zhang, *J Phys Chem* **2022**, *126*, 2587.

[30] B. Wang, X. Wang, P. Wang, T. Yang, H. Yuan, G. Wang, H. Chen, *Nanomaterials* **2019**, *9*, 1706.

[31] Z.-N. Dai, Y. Cao, W. J. Yin, W. Sheng, Y. Xu, *J. Phys. D: Appl. Phys.* **2022**, *55*, 315503.

[32] Z. Mamiyev, N. O. Balayeva, *Catalysts* **2022**, *12*, 1316.

[33] X. Wang, X. Wang, J. Huang, S. Li, A. Meng, Z. Li, *Nat. Commun.* **2021**, *12*, 4112.

[34] T. Hisatomi, K. Domen, *Nat. Catal.* **2019**, *2*, 387.

[35] Q. Wang, T. Hisatomi, Q. Jia, H. Tokudome, M. Zhong, C. Wang, Z. Pan, T. Takata, M. Nakabayashi, N. Shibata, Y. Li, I. D. Sharp, A. Kudo, T. Yamada, K. Domen, *Nat. Mater.* **2016**, *15*, 611.

[36] B. Sun, W. Zhou, H. Li, L. Ren, P. Qiao, W. Li, H. Fu, *Adv. Mater.* **2018**, *30*, 1804282.

[37] S. Wang, B. Y. Guan, X. Wang, X. W. D. Lou, *J. Am. Chem. Soc.* **2018**, *140*, 15145.

[38] S.-S. Yi, J.-M. Yan, B.-R. Wulan, S.-J. Li, K.-H. Liu, Q. Jiang, *Appl. Catal., B* **2017**, *200*, 477.

[39] J. Liu, Y.-H. Guo, Z.-Y. Hu, H. Zhao, Z.-C. Yu, L. Chen, Y. Li, G. Van Tendeloo, B.-L. Su, *Cell Commun Signal* **2023**, *5*, 372.

[40] J. Ran, L. Chen, D. Wang, A. Talebian-Kiakalaieh, Y. Jiao, M. Adel Hamza, Y. Qu, L. Jing, K. Davey, S.-Z. Qiao, *Adv. Mater.* **2023**, *35*, 2210164.

[41] W. Feng, G. Wu, L. Li, N. Guan, *Green Chem.* **2011**, *13*, 3265.

[42] M. M. Momeni, M. Taghinejad, Y. Ghayeb, A. N. Chermahini, R. Bagheri, Z. Song, *Appl. Physic. A* **2021**, *127*, 104.

[43] Y. Shiraishi, S. Kanazawa, A. Tsukamoto, A. Shiro, Y. Sugano, T. Hirai, *ACS Catal.* **2013**, *3*, 2222.

[44] J. Ran, H. Zhang, S. Fu, M. Jaroniec, J. Shan, B. Xia, Y. Qu, J. Qu, S. Chen, L. Song, J. M. Cairney, L. Jing, S.-Z. Qiao, *Nat. Commun.* **2022**, *13*, 4600.

[45] A. Behranginia, P. Yasaei, A. K. Majee, V. K. Sangwan, F. Long, C. J. Foss, T. Foroozan, S. Fuladi, M. R. Hantehzadeh, R. Shahbazian-Yassar, M. C. Hersam, Z. Aksamija, A. Salehi-Khojin, *Small* **2017**, *13*, 1604301.

[46] M. Peng, Y. Ma, L. Zhang, S. Cong, X. Hong, Y. Gu, Y. Kuang, Y. Liu, Z. Wen, X. Sun, *Adv. Funct. Mater.* **2021**, *31*, 2105051.

[47] Y. Liu, D. A. Cullen, T. Lian, *J. Am. Chem. Soc.* **2021**, *143*, 20264.

[48] Y. Yang, W. Rodríguez-Córdoba, T. Lian, *J. Am. Chem. Soc.* **2011**, *133*, 9246.